# Measuring Fluxes of Meteor Showers with the NASA All-Sky Fireball Network

Steven Ehlert[a], Rhiannon Blaauw Erskine[b,c]

[a]*Qualis Corporation, Jacobs Space Exploration Group, NASA Meteoroid Environment Office, Marshall Space Flight Center, Huntsville, AL, USA, 35812*
[b]*Jacobs Space Exploration Group, NASA Meteoroid Environment Office, Marshall Space Flight Center, Huntsville, AL, USA, 35812*
[c]*Department of Physics, Wheaton College, 501 College Avenue, Wheaton, IL, USA 60187*

## Abstract

We present an algorithm developed to measure the fluxes of major meteor showers as observed in NASA's All-Sky Fireball Network cameras. Measurements of fluxes from the All-Sky cameras not only improve the Meteoroid Environment Office's (MEO's) ability to provide accurate risk assessments from major showers, but also allows the mass distribution of meteoroids within the shower to be constrained. This algorithm accounts for the shower-specific and event-specific exposure time and collecting area of the sky for nights where sufficiently large samples of shower meteors ($\sim 30$ or more from the shower) are observed. The fluxes derived from the All-Sky Fireball Network for the 2015 Geminid, 2016 Perseid and Quadrantid, 2017 Orionid, and 2018 Leonid shower peaks are calculated. All five of these shower fluxes show excellent agreement with expectations from independent measurements at different mass and luminosity limits. For four of these five showers, the measured mass indices are significantly shallower than what is currently assumed by the NASA Meteoroid Environment Office's (MEO's) annual meteor shower forecast. A direct comparison between forecasted and measured fluxes at

limiting masses of $\sim 1\,\mathrm{g}$ shows good agreement for the three showers for which the observations took place near their peak activity.

*Keywords:*

Meteoroids, Showers, Video

## 1. Introduction

The meteor shower forecast and Meteoroid Engineering Model (MEM) produced by NASA's Meteoroid Environment Office (MEO) are fundamentally predictions of the number of meteoroids above a given mass threshold that are expected to impact a spacecraft surface during a particular time. This quantity, known as the flux, is the primary driver of spacecraft risk - a higher flux of meteoroids increases the likelihood of impacts and subsequently risk to the spacecraft.

Although flux may be the primary quantity for spacecraft risk, the mass distribution of the meteor shower also plays a role in fully assessing spacecraft risk. Impacts from more massive meteoroids cause more damage to spacecraft. It is therefore imperative to quantify the extent to which a particular meteoroid source may be populated with more massive meteoroids. Such a measurement can be determined using measurements of the flux at different mass limits. Typically, meteoroid masses are assumed to follow a power-law distribution, where the differential number of meteoroids in a given mass bin is given by

$$\frac{dN}{dm} = N_0 \left( \frac{m}{m_\star} \right)^{-s} \tag{1}$$

where $s$ is known as the mass index, and typically takes on values of $s \sim$

2

1.5 − 2.5. The cumulative flux for all meteoroids above a given mass, denoted as $F(> m)$, is proportional to $m^{1-s}$. We normalize the distribution to some arbitrary characteristic mass $m_\star$ in order to maintain clarity in the units of all terms.

Uncertainties in the mass index can greatly influence the potential risk to spacecraft when extrapolating to high masses. If two sources had the same flux at a mass limit of $1\,\mathrm{mg}$ but had mass indexes different by 0.3 (such as 1.7 and 2.0), the source with the lower mass index would have roughly 8 times the flux of the other at a mass limit of $1\,\mathrm{g}$. Since these differences may greatly influence spacecraft design and operations, it is crucial for any model of the meteoroid environment to estimate these mass indices as accurately as possible.

Fluxes may be an important input quantity for the meteor shower forecast and MEM, but the measurement of meteor shower fluxes requires serious observational resources and careful calculations. The MEO has previously measured fluxes only in its Wide-Field camera system (Blaauw et al., 2016a), which observes four separate $15° \times 20°$ regions of the sky for meteors to a limiting mass of $\sim 1\,\mathrm{mg}$. This algorithm refines upon previously published algorithms for measuring calibrated shower fluxes (e.g., Molau and Barentsen, 2013; Ott et al., 2014), but all of these publications calculate fluxes using a process that assumes a relatively small ($\sim 20° - 30°$) field of view. The flux calculation developed for the Wide-Field cameras does not fundamentally depend on the number of meteors detected, and provides measurements even when as few as one shower meteor has been observed.

The MEO has not previously measured fluxes from its All-Sky Fireball

3

Network, which would provide an additional measurement of the flux for showers at a mass limit of $\sim 1\,\mathrm{g}$. This ability would not only provide an independent measure of the flux, but the combined measurements from both camera systems produces a direct measurement of the mass index $s$ across the entire spacecraft threat regime. Meteoroids more massive than $\sim 1\,\mathrm{g}$ are generally too rare to have any appreciable chance of impacting a spacecraft.

The differences in field of view, camera geometry, and number statistics between the All-Sky and Wide-Field systems demand different assumptions and computations. This report will describe how such calculations can be performed for the nights with the highest shower activity using the cameras of the NASA All-Sky Fireball Network. It is crucial to point out that the calculation described in this report can ONLY be performed for meteor showers during their periods of highest activity.

Just as important from the standpoint of spacecraft risk assessment, the process described here will also enable uncertainties on the All-Sky flux and any measurements derived from this flux measurement to be estimated. Throughout this report, all statistical variables are assumed to follow a Gaussian distribution unless otherwise noted, and uncertainties correspond to the central $68.3\%\,(1-\sigma)$ confidence interval.

## 2. Needed Quantities and Assumptions

The measurement of a meteoroid flux from a given source as observed in the All-Sky Fireball Network is defined entirely by four quantities alluded to above. We define them below, and label them with the subscript $i$ when the quantity in question is specific to a single meteor event.

4

1. The number of meteor events detected that satisfy certain quality cuts, $N$.

2. The collecting area of the sky for each event, $A_i$.

3. The total exposure time in which the cameras that detected the event could feasibly observe similar events, $t_i$.

4. The limiting mass/absolute magnitude of the flux measurement, which corresponds to the least massive/luminous meteoroid for which our survey is complete (i.e., where we expect to have observed $\sim 100\%$ of the events that occured over those cameras). We denote the limiting mass and magnitude as $m_{lim}$ and $M_{lim}$, respectively.

The task of any flux measurement is to determine these four quantities as accurately as possible. Whenever relevant, we will compare and contrast the process described here with the Wide-Field algorithm (Blaauw et al., 2016a).

## 2.1. Assumptions

The determination of the four quantities described above inevitably requires a large number of simplifying assumptions to be made about the meteor survey performed. Before discussing the All-Sky flux algorithm in detail, we will first explicitly describe the assumptions we make in these calculations.

1. We have a list of meteors observed within an All-Sky camera network. The information calculated for each event includes, at a minimum: the event date/time; its beginning height, its peak absolute magnitude[1],

---

[1]Unless otherwise noted, the use of the word magnitude in this manuscript corresponds to the peak absolute magnitude of the meteor observed during its ablation.

the cameras in the network that detected it, and a shower identification label.

2. We can estimate a limiting magnitude for the meteors associated with a given meteor shower on a given night across the entire camera network based on the observed distribution of meteor magnitudes.

3. For meteors brighter than this limiting magnitude, the meteor survey is complete for all camera combinations and event times. While we expect certain cameras to be able to observe meteors fainter than this network-wide limiting magnitude at certain times, these fainter meteors are not considered in the flux calculation.

4. Each meteor event has a specific detector volume defined by the combination of cameras that detected it.

5. The detector volume is bound to a range of heights and a minimum elevation angle above the horizon. These same bounds must be satisfied in every camera that detected it. If the meteor event does not satisfy these bounds in a particular camera that detected it, that camera is excluded from consideration in the detector volume calculation.

6. The event-specific detector area that goes into the flux calculation is defined as the projection of this volume along the direction of the local radiant at the event time. This projection operation will be discussed in detail in Section 2.6.

7. The exposure time associated with a particular meteor event is the total time throughout the night where every camera that detected this event could have feasibly detected other meteors. Note this is an "intersection" operation and not a "union" operation (i.e., the total clear

6

time in a pair of cameras is the total time where it is clear in BOTH
cameras simultaneously).

With these assumptions in mind, we will now describe the calculations
for each of these four quantities (number, area, time, and limiting mass) in
detail.

## 2.2. The Meteor Sample

The flux calculations we are performing will only be performed for meteors
that were observed in at least two All-Sky cameras at elevation angles above
30 degrees. This requirement has two purposes: First, it ensures that each
meteor has an accurate atmospheric trajectory and orbit determination; and
it secondly provides a more accurate estimate of the collecting volume of
the sky that is visible to meteoroids. These cuts ensure that the meteoroids
curated for each shower and night constitute a pure sample of shower meteors
with well defined collecting areas. If a meteor event has been observed by
three or more cameras, we consider it to be a detection only in the cameras
where this minimum elevation angle requirement is met.

## 2.3. Limiting Magnitude

Because the determination of All-Sky camera fluxes is limited to nights
with large samples of shower meteors detected, we can infer the limiting
magnitude of the sample directly from the data. The distribution of magnitudes associated with the shower is fit with a Gumbel distribution, following
the methodology of Blaauw et al. (2016a); Kingery and Blaauw (2017). A
Gumbel distribution has a probability distribution function (PDF) of the
form

$$p(x; \mu, \beta)dx = \frac{1}{\beta}e^{-(z+e^{-z})}dx \qquad (2)$$

where the parameter $z$ is defined as $z = \frac{x-\mu}{\beta}$. This choice of PDF has the added convenience that the mode of the PDF is given trivially as $\mu$. We assume that the mode of the best-fit PDF is the limiting magnitude of the shower meteors on that particular night (i.e., $M_{lim} = \mu$). As stated above we assume that our sample of meteors is complete for magnitudes brighter than the limiting magnitude irrespective of the particular cameras that observed it or the time of observation. The distribution of peak absolute magnitudes for Perseid meteors observed on the night of 2016-08-12 and the corresponding best-fit Gumbel distribution to these data is shown in Figure 1. Only one limiting magnitude is determined for the entire observation network during that night - effectively averaging over the selection functions for each camera and observation time.

The Wide-Field fluxes algorithm has enough stars in the field of view that a limiting *stellar* magnitude can be modeled in a similar fashion whenever the skies are clear. This limiting stellar magnitude is then converted into a limiting meteor absolute magnitude by correcting for the range and angular motion of the meteor over the duration of one video frame. A limiting meteor magnitude from a particular meteor shower can therefore be inferred for the Wide-Field cameras even when no meteors from the shower are detected. There are insufficient stars too sparsely distributed across the field of view to properly infer the limiting stellar magnitude in the All-Sky cameras, and the limiting meteor magnitude must therefore be derived from the distribution of meteor absolute magnitudes itself. This is the primary reason why shower
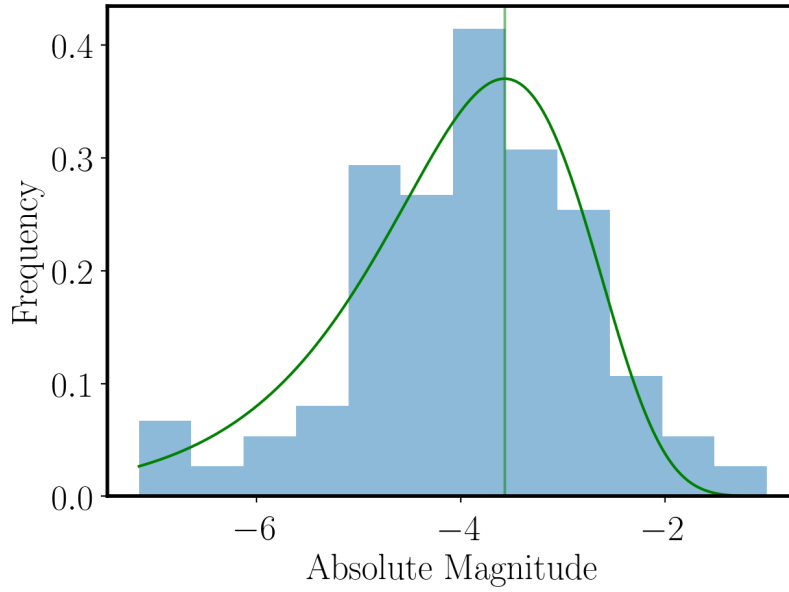
8

Figure 1: The distribution of peak absolute magnitudes for 146 Perseid meteors observed on the night of 2016-08-12. The green curve denotes the best-fit Gumbel distribution to this histogram, which has $\mu = -3.57 \pm 0.10$ and $\beta = 0.99$. The limiting magnitude is calculated as $M_{lim} = \mu$, meaning we expect our Perseid sample to be complete to meteors brighter than magnitude $-3.57$, denoted by the vertical green line.

fluxes can only be measured with All-Sky cameras when large samples of shower meteors are detected.

## 2.4. Detector Volume

We assume that the detector volume of the sky associated with the $i^{th}$ meteor, $V_i$ , is independent of the time of observation. It does, however, depend on the combination of cameras that observed it and the shower in question. We assume that the detector volume covers a range of heights based on the empirical distribution of beginning heights for the meteors. In order to utilize the largest possible range of heights, we set the minimum and maximum heights for the detector volume to the minimum and maximum beginning heights for the entire population of meteors from the shower in question observed by the NASA All-Sky Fireball Network. This includes both meteors observed on the night for which the fluxes are to be calculated as well as any other night where meteors from this shower were observed over the course of the camera network's entire operational lifetime. We restrict the beginning height distribution to only include those events with a convergence angle (Ceplecha, 1987) of greater than 15°, in order to ensure that the meteor events all have well determined trajectories. The distribution for beginning heights of all observed Geminids are shown in Figure 2. Also overlaid on this figure are the assumed minimum and maximum heights for the detector volume.

With the minimum and maximum heights of the detector volume determined, the full detector volume can be defined. We first use the latitudes and longitudes of every camera along with the minimum and maximum heights to determine a series of points in Earth-Centered Earth-Fixed (ECEF) co-
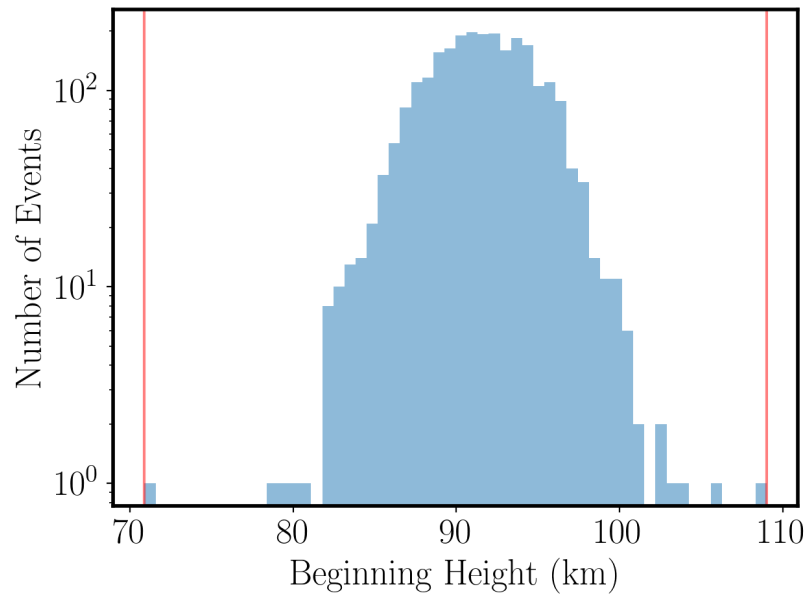
10

Figure 2: The distribution of beginning heights of all Geminid meteors observed over the lifetime of the NASA All-Sky Fireball Network. The outer red lines correspond to the assumed minimum and maximum heights of the sky detector volume for the Geminids.

ordinates. The minimum and maximum values of the ECEF coordinates across all cameras define a large cube that is then discretized into spheres of radius 4 km. The choice of spheres simplifies later calculations, and we will discuss that choice in detail later in this report. We identify the positions (in ECEF coordinates) of spheres that are within the previously determined height range and are at an elevation angle above 30 degrees. We only consider volume elements that are at elevation angles above 30 degrees in every camera. This first restriction is to ensure consistency with our elevation angle cutoff for the meteor event sample. This collecting volume is inevitably smaller for events observed in three or more cameras than for events observed only in two cameras, since the collecting volume is defined as the volume at the intersection of all of the camera fields of view. At the end of this calculation, we have the positions of spheres 4 km in radius that satisfy all of these cuts in every All-Sky camera that observed the event.

## 2.5. Clear Time

For the Wide-Field camera network, stack images combining 40 s of frames are produced every 10 minutes. The distribution of pixel values within these stack frames are measured and used to infer whether the image is clear or cloudy. While the same stack images are produced for each All-Sky camera every 30 minutes, the same analysis procedure cannot be applied to these data. Since these cameras have a field of view that covers the entire sky, single value statistics are largely meaningless. Clouds will likely cover some fraction of the field of view while leaving other regions clear. The Moon will certainly be visible in the field of view whenever it is above the horizon. The illumination levels of these features will vary from site to site as well as

12

seasonally within a single site.

Despite past attempts to develop an algorithmic method of identifying clear and cloudy images in All-Sky cameras, we find that no automated algorithm offers any advantage to visual, manual inspection by a human observer. Since the All-Sky flux algorithm will only be run on nights where there are many meteors detected, the potential concerns of intense and time consuming manual inspection are minimized when the inspection is restricted to these individual nights. Of course, the fact that large samples of meteors were detected on a given night also ensures clear skies were available for at least part of the night.

A graphical user interface (GUI) has been developed to automatically find all of the stack images produced by All-Sky cameras during the night in question and keep track of clear and cloudy times identified by the user. The user simply decides whether a particular stack image (and the 30 minutes surrounding it) should be associated with the clear time or cloudy time based on their best-faith guess as to whether or not a meteor could plausibly be detected in the field of view during that time. The limiting magnitude determination takes into account different seeing conditions for different nights.

## 2.6. Effective Area

Unlike the volume of the sky visible to the intersection of All-Sky cameras between two limiting heights, the area of that volume exposed to the shower radiant changes with time. We calculate the effective area for each event, $A_i$, by projecting the total "detector" volume of the sky along the direction of the radiant. This calculation is greatly simplified by our choice of discretizing the volume into spheres. Since the projected area of a sphere is invariant

13

under rotations $(\pi r^2)$, the only non-trivial calculation is to determine how many spheres are "exposed" to the radiant.

The algorithm we utilize to determine if a particular sphere is exposed to the radiant is as follows: for each sphere center position within the volume, we move two radii away from that point in the direction of the shower radiant. We then calculate the distance to this new point from every sphere point in the sky volume. If the distance to the closest sphere point is greater than 0.7351 times the radius of the sphere itself (nominally 4 km), then we assume that that sphere point is on the exterior of the volume in the direction of the radiant. Otherwise the sphere point is in the interior of the volume. The particular value of 0.7351 was determined using Monte Carlo simulations of this grid setup in order to determine the maximum distance between a step of one diameter in a random direction and the nearest sphere point. As a final correction to the collecting area, we multiply the total cross sectional area of all spheres by a factor of $4/\pi$ to account for the area "missed" by the spheres[2].

The Wide-Field fluxes calculation approaches the collecting area determination differently. It finds the raw area each set of cameras could potentially detect meteors from a specific meteor shower in different height steps since the area changes significantly in the range meteors are detected. These raw areas are then corrected for radiant elevation, camera sensitivity, and other selection effects to become the effective area. By considering the entire volume of the sky visible to the radiant at once as and determining a

---

[2]The ratio of the area of a square to an inscribed circle is $4/\pi$, regardless of the size of the square. This ratio holds even if the square is inscribed by $n \times n$ circles.

14

collecting area independent of the meteor's height of peak emission, we are able to elegantly account for the spherical geometry of the Earth as well as the potentially complex geometry associated with the regions where multiple cameras intersect.

Another crucial difference between the Wide-Field flux calculation and this work is that the Wide-Field calculation is able to account for variations in sensitivity across the sky volume and adjust the areas from individual sky elements to account for those variations. We instead estimate a limiting magnitude to which we expect 100% completeness across the entire camera network. No further corrections to the detector area are therefore necessary at these limiting magnitudes.

## 3. The Shower Flux

The calculations described above provide an event-specific effective area $A_i$ and exposure time $t_i$. These quantities account for the time independent camera geometry, the shower-dependent beginning heights of their associated meteoroids, and the time dependent camera geometry with respect to the shower radiant. We also account for the times during the night when a meteor could be expected to be detected in every camera. With these corrections already determined, we can define the shower flux over a given time period as

$$F(< M_{lim}) = \sum_i \frac{1}{A_i t_i} \tag{3}$$

where $A_i$ is the effective area for the event accounting for both the geometry of all of the cameras that detected that event and the shower geometry. The

15

effective exposure time $t_i$ is the total clear time throughout the night for all of the cameras that observed that event. We emphasize that the total clear time corresponds to an intersection operation and not a union operation - it is the total time throughout the night where the sky was clear over every camera that detected the event.

### 3.1. From Magnitudes to Masses

While the cameras provide a luminosity/absolute magnitude limited flux, the more meaningful quantity from both a physical and engineering standpoint is a mass limited flux. The limiting meteor absolute magnitude is converted into a limiting mass using the luminous efficiency model of Brown (Peterson, 1999) to convert the peak magnitude and entry speed of the meteoroid into a mass

$$2.25 \log_{10} \left( \frac{m_{lim}}{1\,\mathrm{g}} \right) = -8.75 \log_{10} \left( \frac{v}{1\,\mathrm{km\,s^{-1}}} \right) - M_{lim} + 11.59 \qquad (4)$$

which is identical to the luminous efficiency utilized in Blaauw et al. (2016a). This ensures that fluxes with both optical camera systems can be compared directly to one another.

## 4. The Equivalent Zenithal Hourly Rate

In order to compare the measured flux to observations at other sizes/masses, we often compare to other camera systems or different detector instruments. The most consistent source of external data to which we can compare is visual shower counts and Zenithal Hourly Rates (ZHR's). We determine the equivalent ZHR of our measured fluxes at a magnitude of +6.5, which is the standard limiting magnitude for visual observations. We assume that the

16

differential distribution of flux per unit luminosity follows a power law in luminosity, $\mathcal{L}$, which we parameterize as

$$\frac{dF}{d\mathcal{L}} = N_0 \left(\frac{\mathcal{L}}{\mathcal{L}_\star}\right)^{-\alpha} \tag{5}$$

for a characteristic luminosity $\mathcal{L}_\star$. In this parameterization, the luminosity index $\alpha$ is exactly related to the population index of the shower $r$ as

$$\alpha = 1 + 2.5 \log_{10} r \tag{6}$$

This relationship can be extended to a relationship between the population index and mass index through an assumed luminous efficiency. For the luminous efficiency described above, which assumes $\mathcal{L} \propto m^{0.9}$, the mass index is related to the population index as

$$s = 1 + 2.3 \log_{10} r \tag{7}$$

The ratio of the shower fluxes at two different luminosities is given as

$$\frac{F(< M_1)}{F(< M_2)} = \left(\frac{\mathcal{L}_1}{\mathcal{L}_2}\right)^{1-\alpha} \tag{8}$$

and the luminosity ratio can be derived explicitly from the magnitude system as

$$\left(\frac{\mathcal{L}_1}{\mathcal{L}_2}\right) = 10^{(M_1 - M_2)/-2.5} \tag{9}$$

Inserting the empirically determined limiting magnitude as $M_2 = M_{lim}$ and $M_1 = +6.5$ into Equation 9 and the resulting luminosity ratio into Equation 8 allows the corresponding flux at a limiting magnitude of $+6.5$ to be calculated. This flux can be converted into an equivalent ZHR for an assumed population index $r$ using the results of Koschack and Rendtel (1990a,b)

17

$$\text{ZHR} = \frac{F(< +6.5) * 37200\,\text{km}^2}{(13.1r - 16.5)\,(r - 1.3)^{0.748}}.\tag{10}$$

For this work, the fluxes we measure in the All-Sky cameras are supplemented by flux measurements at other limiting masses using a combination of lunar impact monitoring observations, the Wide-Field camera system, and the Canadian Meteor Orbit Radar (CMOR). This combination of measurements provides a direct measurement of the mass index $s$. The empirically determined mass index is then used to determine corresponding values of $\alpha$ and $r$, which subsequently determine the equivalent ZHR value. No independent assumptions about the mass index or flux at a given limiting mass or magnitude are utilized.

## 5. Statistical and Systematic Uncertainties

Just as important as the measurements of the shower flux are the calculations of the expected statistical and systematic fluctuations of that flux measurement. In this section we describe the calculations we perform to estimate these uncertainties.

### 5.1. Limiting Magnitude/Mass Uncertainties

Since the limiting magnitude is determined using an empirical fit to the meteor sample, the uncertainty in the limiting magnitude determination due to small number statistics cannot be ignored. The particular value of the limiting magnitude affects both the limiting mass and flux of the final measurements. We estimate the uncertainty on the limiting magnitude using the covariance matrix of the Gumbel distribution fit. For the five meteor

18

showers we discuss below, we can fit the limiting magnitude to a precision of $\sim 0.1 - 0.6\,\mathrm{mag}$, depending on the size of the underlying sample. Our flux calculation keeps track of the uncertainty in the limiting magnitude as well as the associated uncertainty in the limiting mass using 10,000 Monte Carlo realizations of the limiting magnitude.

*5.2. Flux Uncertainties*

There exist two primary sources of uncertainty in the flux measurement as calculated using equation 3 that are necessary to account for.

1. In the limit of small numbers of meteors detected that have nearly identical area-time products, the Poisson fluctuations on the total number of shower meteors $N$ will dominate. In this case, the uncertainty on the flux can be estimated as $\sqrt{N}/\bar{A}t$, where $\bar{A}t$ is the median area-time product for each meteor event considered in the flux calculation.

2. In the limit of a large meteor sample with large scatter in their individual area-time products, the variance in these area-time products will be the dominant uncertainty in the flux calculation. For this limit, the uncertainty on the flux is best estimated using bootstrap realizations of the sample.

We assume that these two sources of uncertainty are formally independent of one another. The uncertainty in the measured flux associated with the small number fluctuations, $\sigma_{Pois}$, is calculated as

$$\sigma_{Pois} = F/\sqrt{N} \tag{11}$$

which ensures that the *fractional* uncertainty in the flux is equivalent to the *fractional* uncertainty of the underlying sample size, which is itself Poisson

19

distributed. As stated above, bootstrap realizations of the observed sample are utilized to determine the uncertainty associated with the variance in individual event area-time products, $\sigma_{Boot}$. The total uncertainty in the shower flux is given as the sum of these two uncertainties in quadrature, i.e.,

$$\sigma_{Flux}^2 = \sigma_{Pois}^2 + \sigma_{Boot}^2 \tag{12}$$

*5.3. Mass Index Uncertainties*

Mass indices are calculated by fitting the All-Sky fluxes and corresponding fluxes at other limiting masses to a power law model. We determine the uncertainties in the mass index using Monte Carlo simulations that account for the statistical uncertainties in the fluxes at other limiting masses, the uncertainties in the All-Sky flux, and the uncertainties in the limiting mass of the All-Sky flux.

In determining the mass index using the All-Sky fluxes in conjunction with other flux measurements, there is a crucial caveat to this analysis. The Wide-Field and CMOR derived flux measurements themselves assume a nominal mass index. This mass index is necessarily asssumed to account for the differential sensitivity of each sky element. In order to account for this, we allow the other flux measurements to be distributed over a much larger range than the statistical uncertainties would otherwise suggest. The Monte Carlo simulations sample fluxes that are uniformly distributed over a range of $0.5\,$dex, corresponding to a factor of $\sim 3$ in either direction and a fluxes ranging an order of magnitude. This range is also well motivated by the range of physically sensible values of a shower mass index. Since for the other flux calculations the area usually scales as $A^{s-1}$ (e.g. Blaauw et al.,

20

2016b) and the nominally assumed mass index is $s = 2.0$, a $0.5 \, \mathrm{dex}$(? - what is dex) range corresponds to mass index values ranging from $s = 1.5 - 2.5$. The Monte Carlo simulations vary each flux measurement independently of the others.

## 5.4. Equivalent ZHR Uncertainties

Using the same underlying Monte Carlo simulations as those utilized for determining the mass index uncertainties, we calculate the distribution of expected equivalent ZHR's given the uncertainties associated with the mass index, the All-Sky flux, and the limiting mass of the All-Sky flux measurement.

## 6. Results for Five Showers

With the details of this calculation now described, we show the resulting fluxes for All-Sky cameras from several past meteor showers, comparing to other relevant observational data. In particular, the equivalent ZHR's calculated can be compared to observational data from the International Meteor Organization (IMO).

## 6.1. The 2015 Geminid Shower

The Geminid meteor shower as observed on the night of 14-15 December of 2015 provides an extensive data set for calibrating meteor shower flux measurements. On this night, the MEO not only had robust measurements of the shower activity from the Canadian Meteor Orbit Radar (CMOR) and the Wide-Field cameras, but also observed 33 flashes on the lunar surface over a two hour observation period. Given the nominal rate of lunar impacts

21

of $\sim 0.2 - 0.5\,\mathrm{hr}^{-1}$, the vast majority of these flashes are highly likely to be associated with Geminid shower meteoroids.

These three instruments provide Geminid shower fluxes at three different limiting masses that span five orders of magnitude in mass: the CMOR limiting mass is $1.8 \times 10^{-4}\,\mathrm{g}$, while the limiting mass of the lunar impact flashes is $30\,\mathrm{g}$. These three flux measurements were combined in Blaauw (2017) to measure the mass index of the Geminid shower as $s = 1.70$. For the All-Sky calculation, a total of 93 Geminid meteors were observed across the entire All-Sky camera network. Out of this parent sample, 30 of them were brighter than the limiting absolute magnitude of $-2.89$ and above the minimum elevation angle of 30 degrees. With these values, we determine that the All-Sky camera observations had a limiting mass of $2.85\,\mathrm{g}$ and a corresponding flux of $2.04 \times 10^{-5}\,\mathrm{km}^{-2}\,\mathrm{hr}^{-1}$. These measurements, plotted in Figure 3, are in excellent agreement with the expected flux at this limiting mass using the results of Blaauw (2017). The resultant mass index measured with all four instruments is $s = 1.70 \pm 0.07$. This measured mass index value is in excellent agreement with independent measurements of the Geminid mass index using radar observations (Jones and Morton, 1982; Zigo et al., 2009; Blaauw et al., 2011) and visual observations (Arlt and Rendtel, 2006).

Extrapolating the All-Sky flux to the visual magnitude limit of $+6.5$ and this mass index gives an equivalent ZHR of $78 \pm 25\,\mathrm{hr}^{-1}$. The average ZHR value for this time window, as determined by visual observers[3], was $55\,\mathrm{hr}^{-1}$.

---

[3]Specifically, we used the ten time intervals between 00:00 and 12:00 UT on 2015 December 15 presented in the IMO's Visual Meteor Database `https://www.imo.net/members/imo_live_shower?shower=GEM&year=2015`
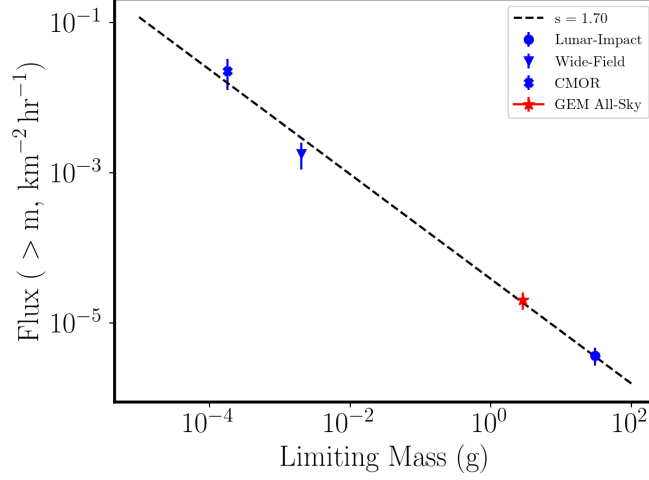
Figure 3: The flux of Geminid shower meteoroids on the night of 2015 December 14/15. The blue markers correspond to the three measurements of Blaauw (2017), while the red star denotes the corresponding All-Sky flux measurement. The black dashed line denotes the best fit mass index of $s = 1.70$.

We reiterate that even for this shower, where we have a prior expectation for the flux within the All-Sky cameras, that the agreement between the equivalent ZHR and that measured by visual observers is not certain.

### 6.2. The 2016 Perseid Shower

Our second example shower flux is derived for the Perseid meteor shower on the night of 2016 August 11/12. We combine this measurement with contemporaneous observations in the Wide-Field cameras and CMOR radar system. A total of 53 Perseid meteors brighter than the limiting magnitude of $-3.34$ were utilized in the flux calculation, derived from a parent sample of 146 Perseid meteors. These numbers result in a flux of $4.86 \times 10^{-5}\,\mathrm{km}^{-2}\,\mathrm{hr}^{-1}$ down to a limiting mass of $0.60\,\mathrm{g}$. Combining this result with the Wide-
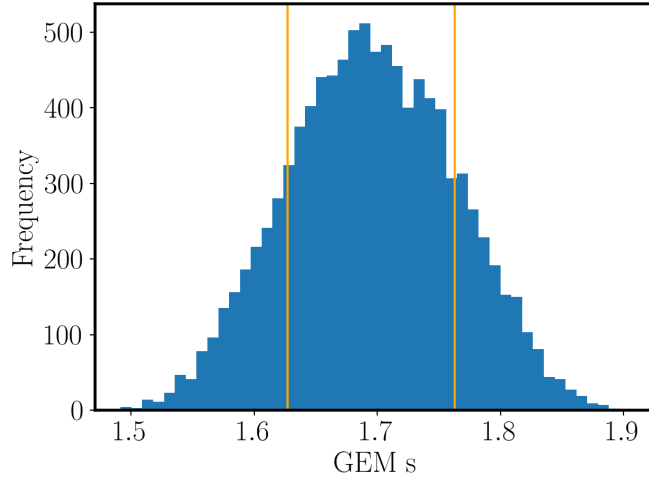
Figure 4: The distribution of Geminid mass indices as determined using Monte Carlo simulations of all four flux measurements and the limiting mass of the All-Sky flux measurement. The vertical orange lines denote the central 68% confidence interval around the best-fit mass index of $s = 1.70$.
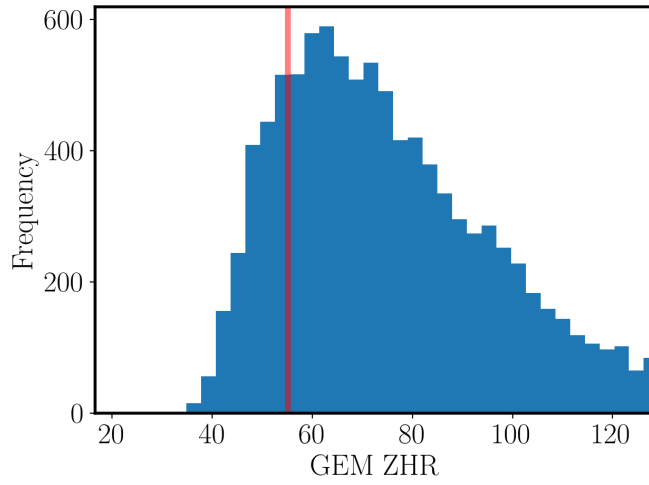


Figure 5: The distribution of equivalent ZHR values at a limiting magnitude of +6.5 for the Geminid meteor shower on the night of 2015 December 14/15. The observed visual ZHR is denoted by the vertical red line.

Field and CMOR fluxes from the same night gives a mass index of $s = 1.54 \pm 0.09$, corresponding to a population index of $r = 1.72$. This mass index is shallower than the lowest Perseid mass indices measured in Hughes (1995), Jenniskens et al. (1998), and Brown (1999), which give typical values of $s \sim 1.7 - 1.8$. Extrapolating the CMOR flux to the limiting All-Sky mass limit assuming a mass index of $\sim 1.8$ results in a flux that is a factor of several lower than what is measured in the All-Sky cameras, however. The mass index measured for the 2016 Perseids is consistent with previously published telescopic observations of the Perseids in 1969 (Krisciunas, 1980) and 1992 (Pravec, 1992). It is possible that the mass index for this year was genuinely shallower than previous encounters due the outbursting nature of the shower during 2016.

We also compare these fluxes to visual observers by calculating the equivalent ZHR. Extrapolating our flux measurement to visual magnitudes of $+6.5$, spanning four orders of magnitude in luminosity, results in an equivalent ZHR of $134 \pm 39 \, \mathrm{hr}^{-1}$. A review of archived visual observations shows that the peak ZHR for this night was $180 \, \mathrm{hr}^{-1}$ and the average visual ZHR during this night[4] was $118 \, \mathrm{hr}^{-1}$.

## 6.3. The 2018 Leonid Shower

Outside of the Perseid and Geminid showers, the single night where the most meteors were detected by the All-Sky Fireball Network was 2018

---

[4]Specifically, we used the fourteen time intervals between 00:00 and 12:00 UT on 2016 August 12 presented in the IMO's Visual Meteor Database `https://www.imo.net/members/imo_live_shower?shower=PER&year=2016`
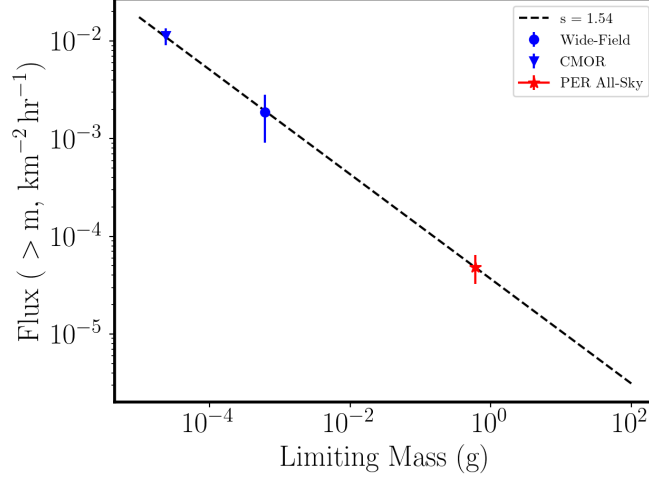
Figure 6: The flux of Perseid shower meteoroids on the night of 2016 August 11/12. The blue markers correspond to the Wide-Field and CMOR flux measurements, while the red star denotes the corresponding All-Sky flux measurement. The black dashed line denotes the best fit mass index of $s = 1.54$.

November 18/19. A total of 15 Leonid meteors out of an initial sample of 38 were brighter than the limiting magnitude of $-3.61$. The corresponding flux is measured as $7.16 \times 10^{-6} \, \mathrm{km}^{-2} \, \mathrm{hr}^{-1}$ down to a limiting mass of $0.43 \, \mathrm{g}$. The equivalent ZHR of this measurement is $37 \pm 17 \, \mathrm{hr}^{-1}$, a value that is in excellent agreement with visual observations of the Leonids during the neighboring nights. The resultant mass index of the Leonid shower across all three instruments is $s = 1.65 \pm 0.09$, which is a value nearly identical to that of the Geminids. This mass index is shallower than that measured by Koten et al. (2011).
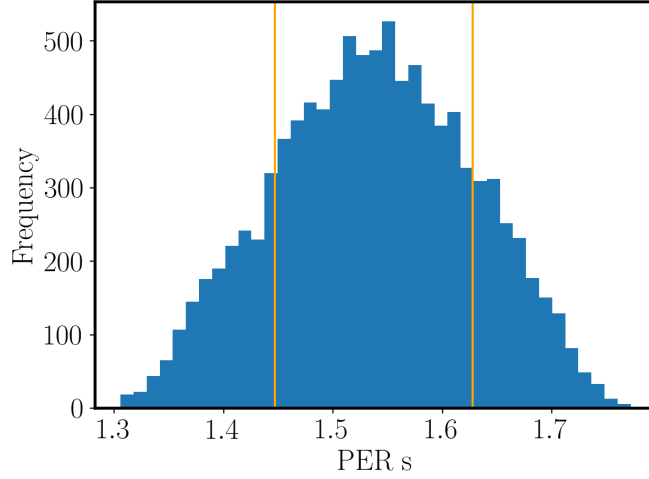
Figure 7: The distribution of Perseid mass indices as determined using Monte Carlo simulations of all four flux measurements and the limiting mass of the All-Sky flux measurement. The vertical orange lines denote the central 68% confidence interval around the best-fit mass index of $s = 1.54$.

## 6.4. The 2016 Quadrantid Shower

We next measure the flux for the Quadrantid shower on the UT date of 2016 January 3/4, with a total of 40 Quadrantid meteors detected across all cameras. Out of these events, a total of 15 Quadrantid meteors are brighter than the limiting magnitude of $-2.56$. The corresponding flux was measured as $1.08 \times 10^{-5} \, \mathrm{km}^{-2} \, \mathrm{hr}^{-1}$ down to a limiting mass of $1.20 \, \mathrm{g}$. Combining this flux with measurements from the Wide-Field cameras and CMOR radar system gives a best fit mass index is $s = 1.83 \pm 0.10$. The equivalent ZHR of this measurement is $63 \pm 33 \, \mathrm{hr}^{-1}$, which is in good agreement with visually observed $ZHR = 33 \, \mathrm{hr}^{-1}$ of the Quadrantids during this night. The mass index of $s = 1.83$ measured here is in good agreement with previous measurements in the radar (Blaauw et al., 2011) and visual observations (Rendtel
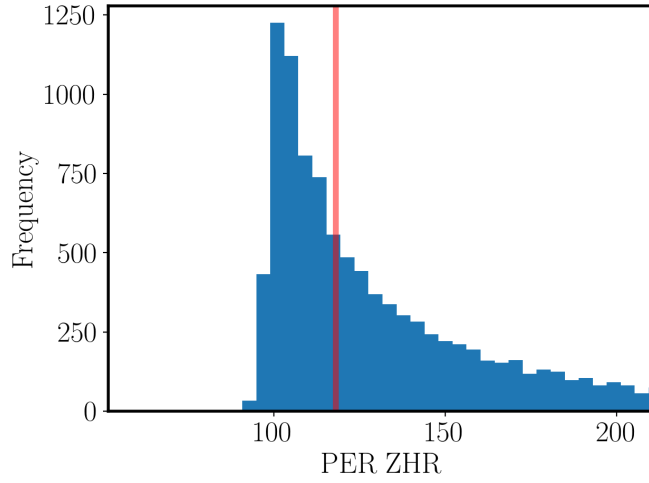
27

Figure 8: The distribution of equivalent ZHR values at a limiting magnitude of +6.5 for the Perseid meteor shower on the night of 2016 August 11/12. This distribution accounts for uncertainties in the flux as measured in the All-Sky cameras, the limiting mass of the All-Sky camera flux measurement, and the mass index. The observed visual ZHR is denoted by the vertical red line. The equivalent ZHR as calculated by an extrapolation over a factor of $\sim 10,000$ in luminosity is in excellent agreement with the visual reports from this same night.
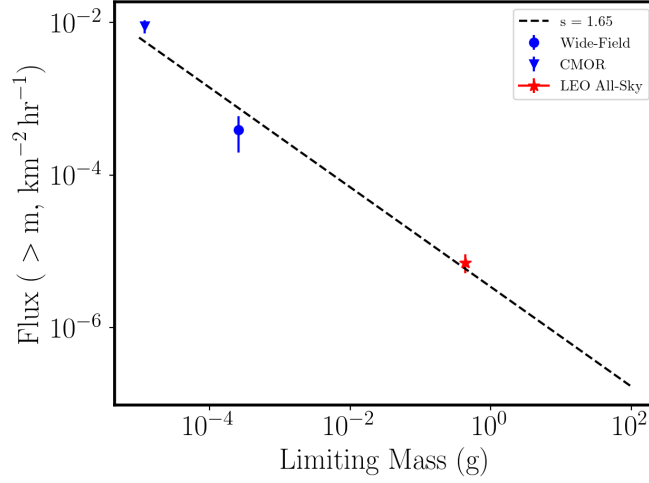
Figure 9: The flux of Leonid shower meteoroids on the night of 2018 November 18/19. The blue markers corresponds to the Wide-Field and CMOR flux measurements, while the red star denotes the corresponding All-Sky flux measurement. The black dashed line denotes the best fit mass index of $s = 1.65$.

et al., 1993; Weiland, 2012).

6.5. The 2017 Orionid Shower

We finally measure the flux for the Orionid shower on the UT date of 2017 October 21/22, with a total of 28 Orionid meteors detected across all cameras. Out of these events, a total of 9 Orionids were brighter than the limiting magnitude of $-3.64$ were identified. The corresponding flux was measured as $4.85 \times 10^{-6}\,\mathrm{km}^{-2}\,\mathrm{hr}^{-1}$ down to a limiting mass of $0.56\,\mathrm{g}$. Combining this flux with contemporaneous measurements from the CMOR radar system gives a best-fit mass index of $s = 1.72 \pm 0.09$. The equivalent ZHR of this measurement is $37\,\mathrm{hr}^{-1}$, with large uncertainties. This value is in good agreement with visually observed $ZHR = 25\,\mathrm{hr}^{-1}$ during this night.
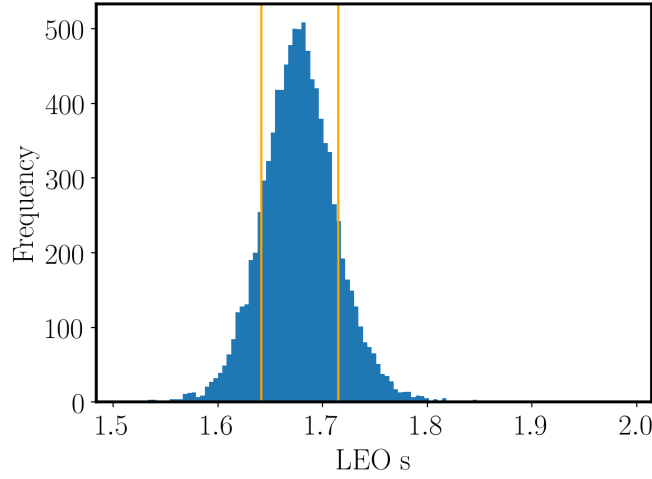
Figure 10: The distribution of Leonid mass indices as determined using Monte Carlo simulations of all four flux measurements and the limiting mass of the All-Sky flux measurement. The vertical orange lines denote the central 68% confidence interval around the best-fit mass index of $s = 1.65$.

The mass index measured in this work is consistent with the results of Jones et al. (1989) and Rendtel (2008), although it is on the low end of values measured by Blaauw et al. (2011).

## 7. Systematic Uncertainties in Sky Geometry

We make one choice about the collecting area of the sky in this flux calculation that requires further justification - an elevation angle cutoff of $30°$. In this section, we discuss how small changes to this otherwise fixed quantity affects the measured All-Sky fluxes for the Geminid meteor shower, the one shower where we have external prior information for both the mass index and ZHR. While it would be ideal to perform this test with additional showers as well, there exist no independent observations for these showers
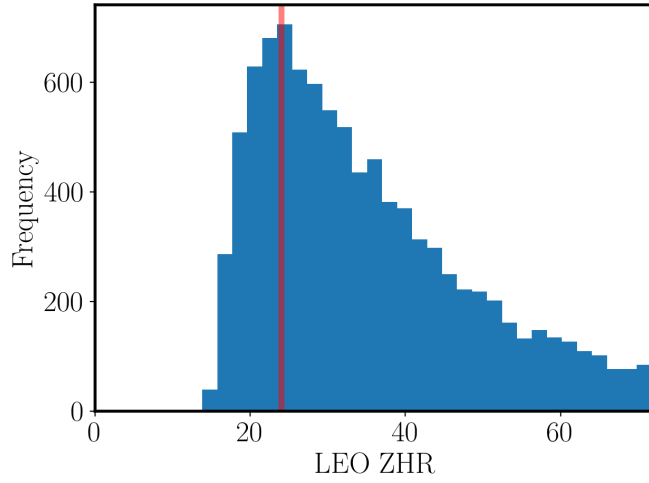
30

Figure 11: The distribution of equivalent ZHR values at a limiting magnitude of +6.5 for the Leonid meteor shower on the night of 2018 November 18/19. This distribution accounts for uncertainties in the flux as measured in the All-Sky cameras, the limiting mass of the All-Sky camera flux measurement, and the mass index. The observed visual ZHR from 2018 November 19/20 is denoted by the vertical red line. The equivalent ZHR as calculated by an extrapolation over a factor of $\sim 10,000$ in luminosity is in excellent agreement with the visual reports from this same night.
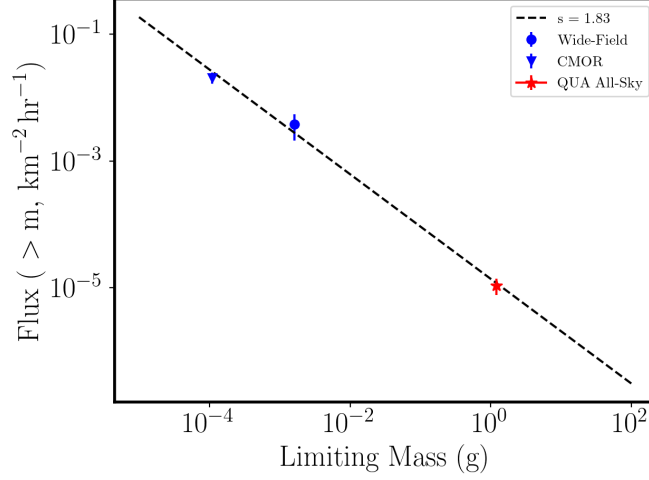
Figure 12: The flux of Quadrantid shower meteoroids on the night of 2016 January 3/4. The blue markers corresponds to the Wide-Field and CMOR flux measurements, while the red star denotes the corresponding All-Sky flux measurement. The black dashed line denotes the best fit mass index of $s = 1.83$.

that can be used to constrain the flux at a limiting mass of $\sim 1\,\mathrm{g}$.

The assumed elevation angle cutoff affects the input meteor sample as well as the collecting area of the calculation. In the ideal case, the measured flux of shower meteors should not depend on the choice of elevation angle cutoff. A stricter elevation angle cutoff should reduce the number of shower meteors by the same factor as the collecting area, leaving the flux invariant. In order to maximize the sample and statistical precision of the measurement, however, the lowest acceptable elevation angle cutoff should be used.

Using the Geminid data from the night of 2015 December 14/15, we show the sensitivity of the flux to the elevation angle cutoff. The results, shown in Figure 18, demonstrate that the flux greatly decreases with decreasing elevation angle cutoff below 30 degrees. Such a trend strongly suggests that
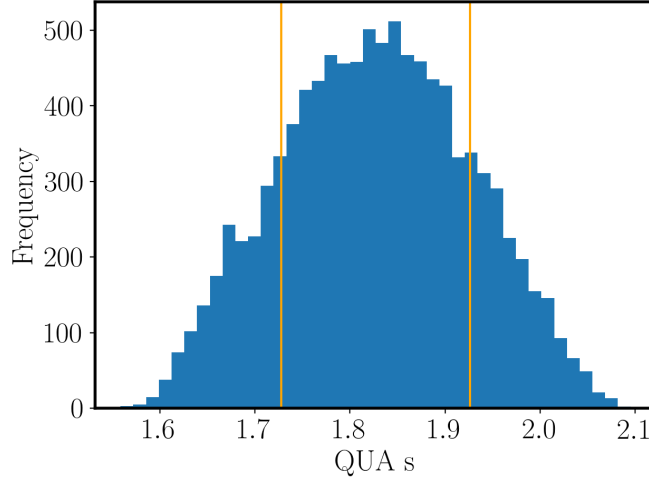
32

Figure 13: The distribution of Quadrantid mass indices as determined using Monte Carlo simulations of all three flux measurements and the limiting mass of the All-Sky flux measurement. The vertical orange lines denote the central 68% confidence interval around the best-fit mass index of $s = 1.83$.

the observed sample of meteors is incomplete at low elevation angles. To avoid such incompleteness concerns, we restrict ourselves to an elevation angle cutoff of 30 degrees.

## 8. Comparisons to the MEO's Shower Forecast

Many of the mass index measurements presented here are for showers whose mass index values are not well established by MEO observations. Instead, nominal values from the IMO or other sources are generally utilized for these showers when creating the annual meteor shower forecast (Moorhead et al., 2017). We compare the three sets of mass indices in Table 1. For four of the five showers, the measured mass indices are lower than those in the shower forecast.
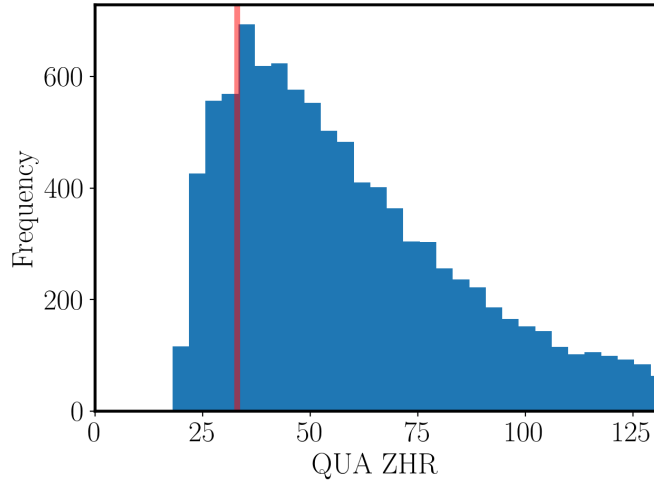
Figure 14: The distribution of equivalent ZHR values at a limiting magnitude of +6.5 for the Quadrantid meteor shower on the night of 2016 January 3/4. This distribution accounts for uncertainties in the flux as measured in the All-Sky cameras, the limiting mass of the All-Sky camera flux measurement, and the mass index. The observed visual ZHR from 2016 January 3/4 is denoted by the vertical red line. The equivalent ZHR as calculated by an extrapolation over a factor of $\sim 10,000$ in luminosity is in excellent agreement with the visual reports from this same night.
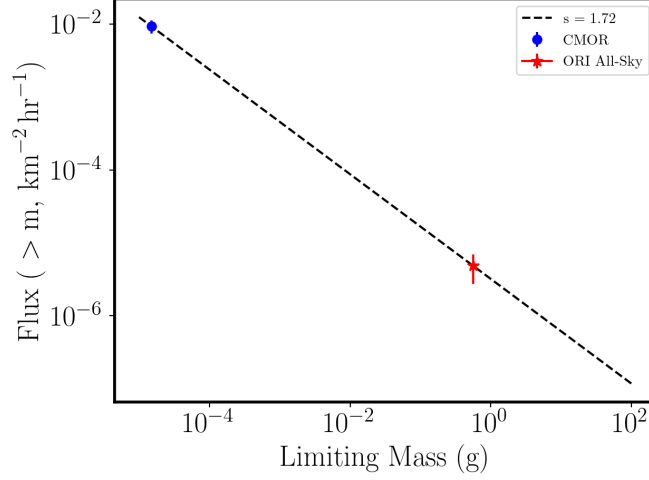
Figure 15: The flux of Orionid shower meteoroids on the night of 2017 October 21/22. The blue circle corresponds to the CMOR flux measurement, while the red star denotes the corresponding All-Sky flux measurement. The black dashed line denotes the best fit mass index of $s = 1.72$.

The forecasted flux on a given date to a given limiting mass depends on more variables than the mass index alone, however. In order to provide the most direct comparison between the model predictions and the observations, we utilize the MEO's past meteor shower forecasts to determine how well they predicted the flux on each of the five nights where shower fluxes were measured. These results are shown in Table 2. The predicted fluxes for all five showers are broadly consistent with the measurements given the statistical uncertainties of $\sim 25 - 50\%$ on the measurements. The flux measurements for the Leonid and Quadrantid showers occurred at dates significantly offset from the peak solar longitude assumed by the shower forecast. Since the assumed activity profile is assumed to follow a double-exponential form (Moorhead et al., 2017), small uncertainties in the activity profile parameters can lead
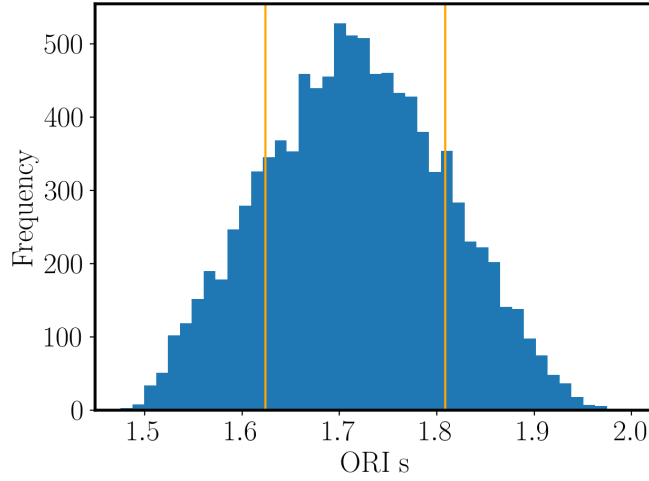
Figure 16: The distribution of Orionid mass indices as determined using Monte Carlo simulations of all three flux measurements and the limiting mass of the All-Sky flux measurement. The vertical orange lines denote the central 68% confidence interval around the best-fit mass index of $s = 1.72$.

to larger uncertainties in the predicted flux at off-peak dates and times.

## 9. Discussion and Future Prospects

The process described here constitutes one of the first algorithms developed to measure calibrated fluxes (number of meteors per unit area and time down to a limiting mass) from All-Sky video cameras. The results from five showers demonstrate that these fluxes are fully consistent with expectations from independent observations in different mass regimes. No special "fine-tuning" of parameters beyond the elevation angle cutoff were performed. The joint measurements of all detectors provide important constraints on the mass indices of meteor showers. We emphasize that the nominal mass limits of the All-Sky and Wide-Field camera networks span the majority of
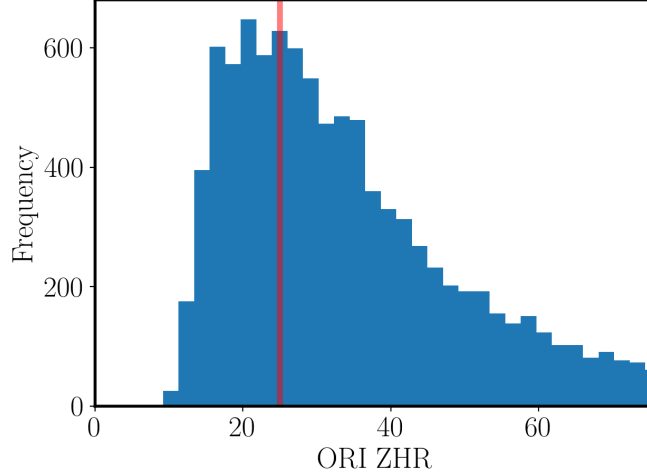
36

Figure 17: The distribution of equivalent ZHR values at a limiting magnitude of +6.5 for the Orionid meteor shower on the night of 2017 October 21/22. This distribution accounts for uncertainties in the flux as measured in the All-Sky cameras, the limiting mass of the All-Sky camera flux measurement, and the mass index. The observed visual ZHR from this same night is denoted by the vertical red line. The equivalent ZHR as calculated by an extrapolation over a factor of $\sim 10,000$ in luminosity is in good agreement with the visual reports from this same night.

| Shower | IMO (r/s) | Forecast (r/s) | This Work (r/s) |
|---|---|---|---|
| Geminids | 2.6/1.95 | 2.6/1.95 | 2.01/1.70 |
| Perseids | 2.4/1.87 | 2.2/1.79 | 1.72/1.54 |
| Leonids | 2.5/1.92 | 2.9/2.06 | 1.92/1.66 |
| Quadrantids | 2.1/1.74 | 2.1/1.74 | 2.30/1.83 |
| Orionids | 2.5/1.92 | 2.5/1.92 | 2.06/1.72 |

Table 1: A comparison between the meteor shower mass and population indices measured in this work with those currently assumed by the IMO and what was assumed in the MEO's annual shower forecast for the year in question (Moorhead et al., 2017).
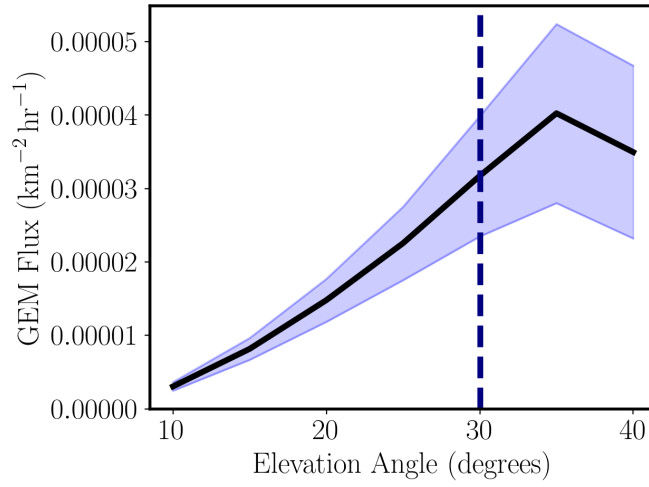
Figure 18: The sensitivity of the measured Geminid shower flux as a function of the minimum elevation angle cutoff. The cutoff chosen for this work, 30 degrees, is denoted by dashed line. For more restrictive cutoffs (above 30 degrees) the flux is consistent with a constant value, whereas a clear decrease in flux is observed for more generous elevation angle cutoffs. This is precisely the trend we expect when the observed sample of meteors at low elevation angles is incomplete.

| Shower | Flux (Forecast) | Flux (This Work) | $B|\lambda_\odot - \lambda_0|$ |
|---|---|---|---|
| Geminids | $2.04 \times 10^{-5}$ | $1.64 \times 10^{-5}$ | 0.21 |
| Perseids | $4.86 \times 10^{-5}$ | $3.46 \times 10^{-5}$ | 0.09 |
| Leonids | $7.16 \times 10^{-6}$ | $4.85 \times 10^{-6}$ | 0.59 |
| Quadrantids | $1.08 \times 10^{-5}$ | $6.90 \times 10^{-6}$ | 0.85 |
| Orionids | $4.85 \times 10^{-6}$ | $3.87 \times 10^{-6}$ | 0.07 |

Table 2: A comparison between the meteor shower fluxes as predicted by the MEO's annual shower forecast and those measured in this work. For all fluxes, the units of flux are $\text{km}^{-2}\,\text{hr}^{-1}$. The fourth column denotes the difference between the solar longitude of the flux measurements and solar longitude of peak activity, normalized by the assumed characteristic scale time of the activity profile $B$ (for more details see Moorhead et al., 2017). Increasing values of $B|\lambda_\odot - \lambda_0|$ are sampling further into the "tails" of the assumed shower activity profile where the observations and model predictions become more uncertain.

the masses that pose risk to spacecraft ($\sim 10^{-3}\,\text{g} - 1\,\text{g}$). When combined with CMOR radar observations (with limiting masses of $\sim 10^{-4}\,\text{g}$,) fluxes across the entirety of the spacecraft threat regime (in terms of meteoroid mass) can be inferred.

The biggest limitation of this analysis procedure is the need to derive the limiting magnitude directly from the observed distribution of shower meteors from that night. While a method to determine the limiting meteor magnitude from the stars or some other independent source of measurements would be preferred, even small uncertainties in the selection function could lead to large uncertainties in the flux. The current method, while only feasible for the most active nights, is robust to systematic uncertainties since it already takes the selection function into account. The selection function is only

taken into account on average across all cameras and times during the night, however, given the sample sizes needed for this analysis to be feasible. A larger number of cameras or a sample of more sensitive cameras may also help boost sample sizes. Given the realities of the observed sample sizes for these five showers, we don't expect there to be many more showers for which fluxes can be measured in this fashion with the All-Sky camera data. By design, however, these five showers are among the most active at masses of $\sim 1\,\mathrm{g}$, and subsequently constitute the showers that pose the most risk to spacecraft.

In addition to requiring that the limiting magnitude of the shower sample be determined empirically, a large sample of shower meteors is also required to ensure that the surviving sub-sample is sufficiently large to provide meaningful results. For these five showers, approximately 50% of the meteors are fainter than the limiting magnitude and are subsequently excluded from any flux calculation. Measuring the flux associated with events fainter than the limiting magnitude requires a full calculation of the selection function, however.

The statistical nature of this procedure also hinders the time scales over which the flux can be measured. This current technique can currently only provide a single flux measurement for a given night. If there are prior reasons to suspect that the shower flux may change significantly over the course of a single night, then that temporal structure cannot be investigated using these algorithms. The practical implications of this limitation on spacecraft risk assessment will inevitably depend strongly on the particular spacecraft's operational constraints.

This work has also shown that, at least for these five showers, well calibrated visual meteor shower observations remain a powerful data source for the MEO. The excellent agreement between the equivalent ZHR for our All-Sky fluxes and measured visual ZHR for all five showers discussed here was essential to validating the general procedure and camera fluxes. Given the huge difference in limiting magnitude for the All-Sky camera fluxes and the visual observers[5], even small systematic errors in the mass/population index, limiting mass, or overall flux could result in largely discrepant extrapolated ZHR's. This procedure also suggests that a power-law distribution across this huge range of luminosities is a reasonable approximation to the shower mass distribution. Showers other than these five may not follow a power-law distribution over such a large dynamic range, however. Comparisons between visual ZHR measurements, Wide-Field fluxes, and All-Sky fluxes could be used, at least in principle, to identify showers where the mass distribution deviates from a power law over this mass range.

Although the mass index values for each of these five showers differs from what has been utilized in past meteor shower forecasts, the agreement between the predicted fluxes and measurements for these five showers are in very good agreement. Our analysis shows that while the All-Sky fluxes and mass indices measured here may improve future forecasts, accurate shower activity profiles can be just as important to predictions of shower fluxes at limiting masses of $\sim 1\,\mathrm{g}$.

Despite these limitations, the ability to measure fluxes and mass indices

---

[5]Approximately 9-10 magnitudes, corresponding to a factor of $\sim 10,000$ in luminosity.

from the All-Sky cameras greatly enhances their ability to inform the shower forecast and MEM. A joint All-Sky, Wide-Field, and CMOR flux analysis could be performed for every night with sufficient numbers of shower meteors, which would improve overall measurement precision and allow the MEO to monitor for variability in both activity and mass indices. All of these measurements would ultimately provide crucial new constraints and insights into the risk major meteor showers pose to spacecraft.

## Acknowledgements

Arlt, R., Rendtel, J., 2006. The activity of the 2004 Geminid meteor shower from global visual observations. MNRAS 367, 1721–1726. doi:`10.1111/j.1365-2966.2006.10077.x`.

Blaauw, R.C., 2017. The mass index and mass of the Geminid meteoroid stream as determined with radar, optical and lunar impact data. Planetary and Space Science 143, 83–88. doi:`10.1016/j.pss.2017.04.007`.

Blaauw, R.C., Campbell-Brown, M., Kingery, A., 2016a. Optical meteor fluxes and application to the 2015 Perseids. MNRAS 463, 441–448. doi:`10.1093/mnras/stw1979`.

Blaauw, R.C., Campbell-Brown, M., Kingery, A., 2016b. Optical meteor fluxes and application to the 2015 Perseids. MNRAS 463, 441–448. doi:`10.1093/mnras/stw1979`.

Blaauw, R.C., Campbell-Brown, M.D., Weryk, R.J., 2011. A meteoroid stream survey using the Canadian Meteor Orbit Radar - III. Mass distribution indices of six major meteor showers. MNRAS 414, 3322–3329. doi:`10.1111/j.1365-2966.2011.18633.x`.

Brown, P.G., 1999. Evolution of two periodic meteoroid streams: The Perseids and Leonids. Ph.D. thesis. THE UNIVERSITY OF WESTERN ONTARIO (CANADA).

Ceplecha, Z., 1987. Geometric, dynamic, orbital and photometric data on meteoroids from photographic fireball networks. Bulletin of the Astronomical Institutes of Czechoslovakia 38, 222–234.

Hughes, D.W., 1995. The Perseid Meteor Shower. Earth Moon and Planets 68, 31–70. doi:`10.1007/BF00671498`.

Jenniskens, P., Betlem, H., de Lignie, M., Ter Kuile, C., van Vliet, M.C.A., van 't Leven, J., Koop, M., Morales, E., Rice, T., 1998. On the unusual activity of the Perseid meteor shower (1989-96) and the dust trail of comet 109P/Swift-Tuttle. MNRAS 301, 941–954. doi:`10.1046/j.1365-8711.1998.02020.x`.

Jones, J., McIntosh, B.A., Hawkes, R.L., 1989. The age of the Orionid meteoroid stream. MNRAS 238, 179–191. doi:10.1093/mnras/238.1.179.

Jones, J., Morton, J.D., 1982. High-resolution radar studies of the Geminid meteor shower. MNRAS 200, 281–291. doi:10.1093/mnras/200.2.281.

Kingery, A., Blaauw, R.C., 2017. Determination of the meteor limiting magnitude. Planetary and Space Science 143, 67–70. doi:10.1016/j.pss.2017.03.006.

Koschack, R., Rendtel, J., 1990a. Determination of spatial number density and mass index from visual meteor observations (I). WGN, Journal of the International Meteor Organization 18, 44–58.

Koschack, R., Rendtel, J., 1990b. Determination of spatial number density and mass index from visual meteor observations (II). WGN, Journal of the International Meteor Organization 18, 119–140.

Koten, P., Borovička, J., Kokhirova, G.I., 2011. Activity of the Leonid meteor shower on 2009 November 17. A&A 528, A94. doi:10.1051/0004-6361/201016212.

Krisciunas, K., 1980. The luminosity functions of the 1969 Perseid and Orionid meteor showers. Icarus 43, 381–384. doi:10.1016/0019-1035(80)90182-7.

Molau, S., Barentsen, G., 2013. Meteoroid stream flux densities and the zenith exponent, in: Gyssens, M., Roggemans, P. (Eds.), Proceedings of the International Meteor Conference, 31st IMC, La Palma, Canary Islands, Spain, 2012, pp. 11–17.

Moorhead, A.V., Cooke, W.J., Campbell-Brown, M.D., 2017. Meteor shower forecasting for spacecraft operations. 7th European Conference on Space Debris 7, 11.

Ott, T., Drolshagen, E., Koschny, D., Drolshagen, G., Poppe, B., 2014. Meteoroid flux determination using image intensified video camera data from the CILBO double station, in: Rault, J.L., Roggemans, P. (Eds.), Proceedings of the International Meteor Conference, Giron, France, 18-21 September 2014, pp. 23–29.

Peterson, G., 1999. Dynamics of Meteor Outbursts and Satellite Mitigation Strategies. The Aerospace Press.

Pravec, P., 1992. Telescopic observations of the 1991 Perseids in Czechoslovakia. WGN, Journal of the International Meteor Organization 20, 46–49.

Rendtel, J., 2008. The Orionid Meteor Shower Observed Over 70 Years. Earth Moon and Planets 102, 103–110. doi:10.1007/s11038-007-9192-0.

Rendtel, J., Koschack, R., Arlt, R., 1993. The 1992 Quadrantid meteor shower. WGN, Journal of the International Meteor Organization 21, 97–109.

Weiland, T., 2012. A rare opportunity: Observing the 2011 Quadrantid maximum from Austria. WGN, Journal of the International Meteor Organization 40, 171–175.

Zigo, P., Porubčan, V., Cevolani, G., Pupillo, G., 2009. The activity and mass distribution of the Geminid meteor shower of 1996-2007 from forward

scatter radio observations. Contributions of the Astronomical Observatory

Skalnate Pleso 39, 5–17.